Direct visualization of electrochemical reactions and comparison of commercial carbon papers *in operando* by fluorescence microscopy using a quinone-based flow cell

Andrew A. Wong, Michael J. Aziz, Shmuel M. Rubinstein

John A. Paulson School of Engineering and Applied Sciences, Harvard University, Cambridge, Massachusetts 02138, USA

We demonstrate the use of fluorescence microscopy as a tool for mapping the spatial distribution of fluid flow and electrochemical reactions in an operating aqueous quinone flow cell. 9,10-anthraquinone-2,7-disulfonic acid (AQDS) is a reversibly redox active molecule with a reduced form (H_2AQDS) that fluoresces when excited by UV light. Visualization of AQDS/H_2AQDS within commercial porous carbon electrode papers enables a direct quantitative comparison of their performance. In particular, this technique illuminates surprisingly large-scale heterogeneous fluid flow profiles present in several carbon papers, leaving substantial areas of the electrode mass-transport limited. In others, more homogeneous flow distribution is observed, but limitations such as low electronic conductivity and limited accessible electrode surface area limit the performance. These observations provide insights into improving structural properties of porous electrodes for high-power density electrochemical flow cells.

Introduction

As the costs of renewable yet intermittent energy generation continue to fall, electrochemical systems, such as flow batteries, have gained attention for potential deployment as grid-scale energy storage units. Significant work has been and continues to be done to improve the performance and, ultimately, decrease the costs for flow batteries: adopting inexpensive, earth abundant aqueous-soluble active materials, developing highly-selective, high-conductivity inexpensive ion exchange membrane (IEMs) or separators, and modifying commercial electrodes for high conductivity, high surface, and catalytic properties[1–4]. However, the improvements to each of these components often lack a deeper understanding of their overlap, namely the fluid flow and electrochemical reaction distribution of active species within porous electrodes. *In situ* techniques, such as fluorescence microscopy, can be used to illuminate these micro-scale phenomena and shed light on opportunities to improve electrochemical flow system performance[5].

In much of the aqueous flow battery research to date, commercial carbon materials in the form of felts, cloths and papers, have been the preferred electrodes due to their high electronic conductivity, high surface area, chemical and mechanical stability, and inhibition of water electrolysis. There exist a number of schemes for thermal[6], chemical[7] and electrochemical pretreatments, and modifications such as laser perforation[8], carbon nanotube decoration[9] and catalyst growth[10] to enhance the electrode surface area[11], catalytic properties[12], and wettability[13]. However, all of these electrode preparation and enhancement procedures start with carbon electrodes produced by relatively few vendors,

and most analyses and cell designs assume these electrodes behave as ideal homogeneous, isotropic, biphasic porous materials. Some significant research has been done to measure and model the properties of these porous electrodes *ex situ*[14,15] which indicates that a homogeneous model is unlikely to be completely accurate. However, direct *in situ* measurements on the scale of the electrode fibers and pores has been lacking in the field.

In the past few years, aqueous soluble organic molecules, such as quinones, have been increasingly studied because of their potential use as abundant, inexpensive active electrolytes for flow batteries[16–19]. Beneficially, redox-active quinones can also have distinct fluorescence signatures between their oxidized and reduced states[20]; this enables direct, *in situ*, electrochemical reaction-fluid flow mapping of the active electrolytes by light-based techniques such as fluorescence microscopy. In contrast to other *in situ* techniques used to characterize flow batteries[21], fluorescence microscopy enables fast (<100 ms), high resolution (<10 μm) imaging over large areas enabling a detailed understanding of the electrolyte-electrode interaction.

In this work, we use fluorescence microscopy to illuminate the reaction-flow properties of a quinone flow cell *in operando* using several different commercial carbon papers as the porous electrode. The results suggest that carbon electrodes can be surprisingly heterogeneous on scales relevant to flow cell operation; this heterogeneity can lead to a non-uniform fluid flow distribution and a diminished utilization of the full electrode surface area. This insight provides an opportunity for exploring improved electrode architectures and engineering high-performance porous electrodes for electrochemical flow systems.

Experimental

A homemade quinone-hydrogen flow cell (QHFC) is used for all fluorescence microscopy experiments. A schematic for this setup and a photograph of the assembled cell are depicted in Figure 1. The negative terminal is plumbed with a pressurized, humidified hydrogen source regulated to an inlet pressure of 5 psi. Hydrogen is oxidized at the 5 cm^2 negative electrode (Pt-C reformate anode from Alfa Aesar) compressed against a stainless steel current collector with a grooved serpentine flow field to enable excess liquid removal. The positive terminal is plumbed with 10 mM 9,10-anthraquinone-2,7-disulfonic acid (AQDS, ion exchanged from TIC America anthraquinone-2,7-disulfonic acid disodium salt) in 1 M H_2SO_4, called the posolyte. AQDS is reduced to H_2AQDS in a 5 cm^2 porous carbon electrode compressed against a gold wire current collector. A Nafion 212 cation exchange membrane (CEM) is used to separate the two half-cell reactions. An interdigitated flow field is milled out of 3/16" UV-transparent acrylic (clear U.V.T. acrylic, EMCO Industrial Plastics) and assembled on top of the positive terminal to enable direct visualization with microscopy.

Four different commercial carbon papers are used for the positive electrode: Sigracet 10AA, 34AA and 39AA (SGL Carbon), and Toray 060. The Sigracet carbon papers are pretreated by baking at 400°C in air for 24 hours, and the Toray 060 is pretreated by chemical etching in 1:3 (v:v) mixture of concentrated nitric and sulfuric acids for 5 hours at 50°C following the procedure described by Chen *et al.*[18]

All of the electrochemistry is performed by a Gamry Reference 3000 Potentiostat and the posolyte is circulated by a peristaltic pump (Cole Parmer, MasterFlex). In each experiment, the potential is held at 0 V to enable the spontaneous oxidation of H_2 (g) and reduction of AQDS (l). The full assembly is imaged by fluorescence microscopy (Axio Zoom V.16, Filter Set 02, Plan Neofluar 1x objective) with a 50 fps capture rate.

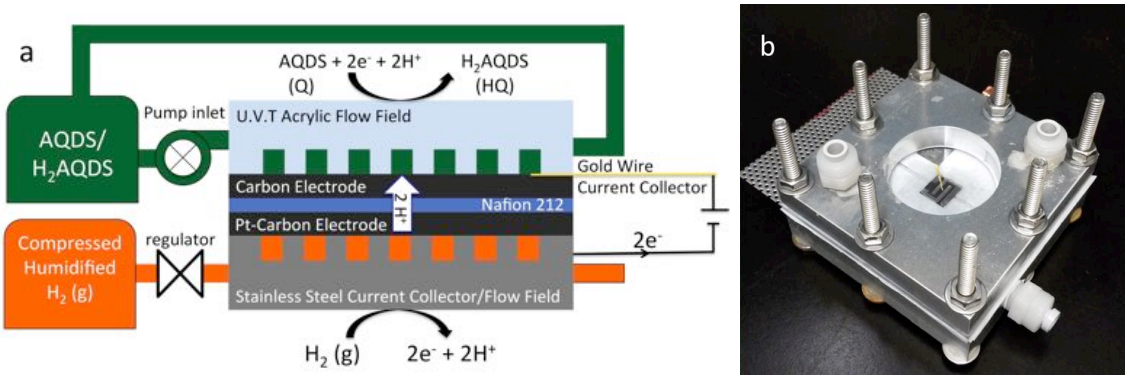

Figure 1. (a) Schematic and materials for the quinone-hydrogen flow cell (QHFC) used throughout this work. The posolyte reservoir starts at 100% AQDS for all experiments. (b) Photograph of assembled QHFC with viewing window to enable bright field and fluorescence microscopy.

Results and Discussion

Scanning Electron Microscopy

Figure 2 shows SEM micrographs of SGL10AA, SGL 39AA and Toray 060 all at the same magnification. Generally, carbon filaments are 10-20 μm in diameter with pore diameters on the order of 50 μm in diameter. From the SEM images, it is clear that the filament morphology and overlaps differ noticeably between carbon papers, in particular with the SGL 10AA containing looping filaments whereas the SGL 39AA and Toray 060 have long, straight filaments—these filaments often span beyond centimeter length scales. SGL 34AA, which is not imaged, has similar morphology to SGL 39AA. Table 1 gives the physical properties of each porous carbon paper electrode according to the vendor data sheets. While bulk properties such as porosity are averaged over the whole electrode area, it is clear from the SEM images that physical phenomena on the millimeter scale will be influenced by local properties. For systems such as flow batteries, the electrode thickness and interdigitated inlet-outlet spacing are on this length scale.

The commercial carbon papers are assembled into the QHFC positive terminal with Teflon spacers to slightly compress them against the U.V.T. acrylic flow plate. Figure 3 depicts a top view of the 2 cm^2 interdigitated flow field (IDFF) and outlines the field of view for the subsequent results and discussion. Though there are several different flow field designs for electrochemical flow systems, IDFF was selected in order to image the total fluid flow through lands of the electrode because it is difficult to image through the channels. This configuration prevents fluid from bypassing the electrode as happens in flow-by designs. As will be demonstrated in this work, the flow field design and the electrode morphology will influence the fluid-flow and electrochemical reactions expected to affect the ultimate device performance.

TABLE I. Comparison of porous carbon paper electrode physical properties. *Asterisk indicates own measurement

Physical Property	SGL 10AA	SGL 34AA	SGL 39AA	Toray 060
Thickness (μm)	390	280	280	190
Porosity (%)	82	75	89	78
Through-Plane Area-Specific Resistance ($m\Omega cm^2$)	<16	<14	<5	80
Fiber Diameter (μm)*	10	8	8	10

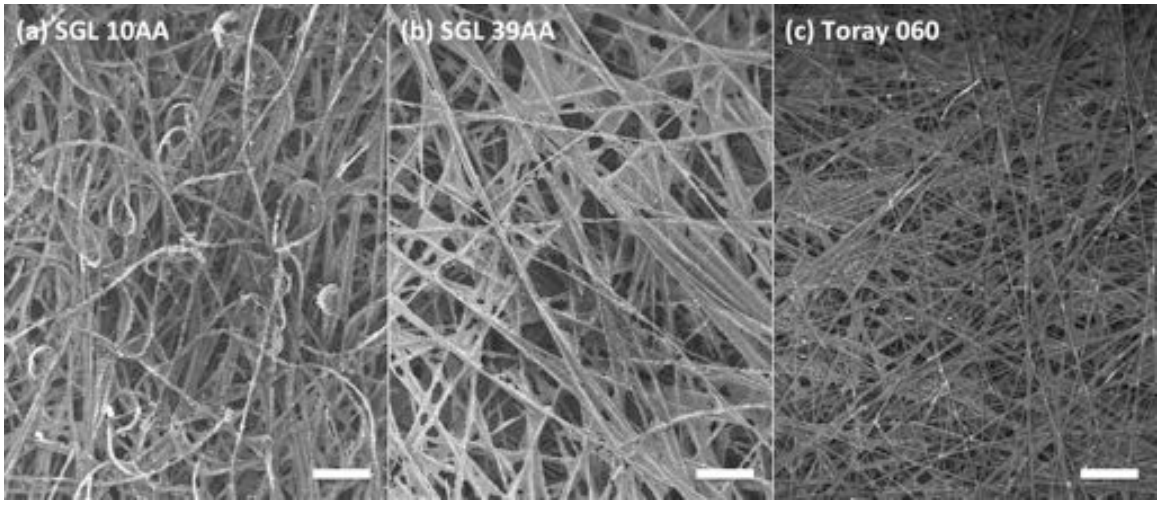

Figure 2. SEM images of three of the porous carbon paper electrodes: (a) SGL 10AA, (b) SGL 39AA and (c) Toray 060. All scale bars are 100 μm.

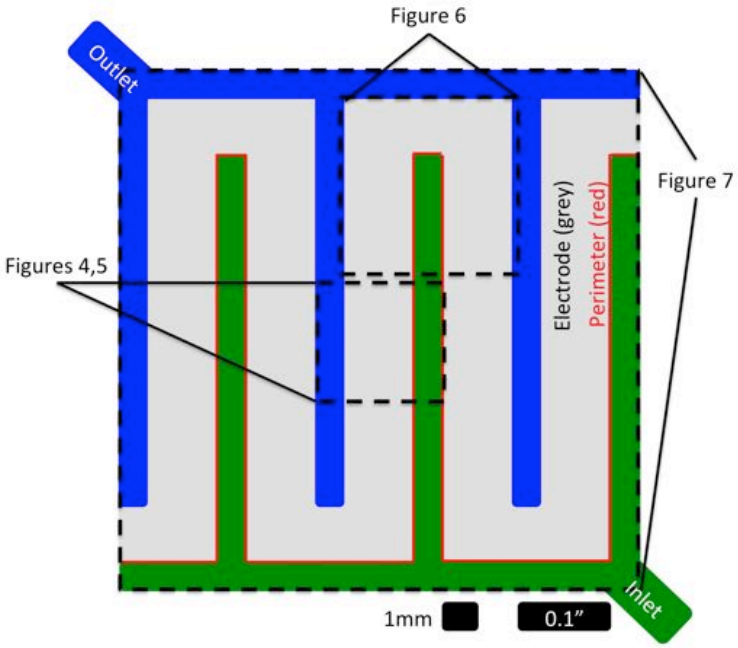

Figure 3. Schematic of the 2 cm^2 IDFF milled out of U.V.T. acrylic on the positive terminal. Dashed regions indicate the field of view for the subsequent figures in this paper.

Fluorescence Microscopy

The peristaltic pump used in this experiment creates a natural pulsation, which dynamically changes the inlet pressure and fluid flow rate with an observable effect. Figure 4 shows the fluorescence microscopy images for the four commercial electrodes during pump pulse starting at the top (a, e, i, and m) with a stagnant resting phase and steadily moving to a maximum fluid flow velocity phase (d, h, l, and p). All fluid flow starts at the inlet channel (right) and traverses underneath the land through electrode to the outlet channel (left). AQDS is electrochemically reduced to H_2AQDS by holding the cell at 0 V throughout the experiment. H_2AQDS is the fluorescent species, so all of the bright areas indicate regions of high concentrations of the reduced species. These

fluorescence microscopy images reveal that fluid flow and steady state electrochemical reactions are not uniform throughout the electrodes. The progression for SGL 10AA from a stagnant, H_2AQDS-filled electrode image (Fig. 4(a)) to a flowing, AQDS-refreshing image (Fig. 4(d)) suggests these papers are surprisingly heterogeneous in their properties. The horizontal banding of bright and dark regions indicate local fluid flow channels on the order of <100 μm are forming between the inlet and outlet channels. The very bright regions in the upper left of these images suggest regions of stagnant flow where reduced H_2AQDS is not being replenished by the advection of oxidized AQDS and is therefore diffusion limited.

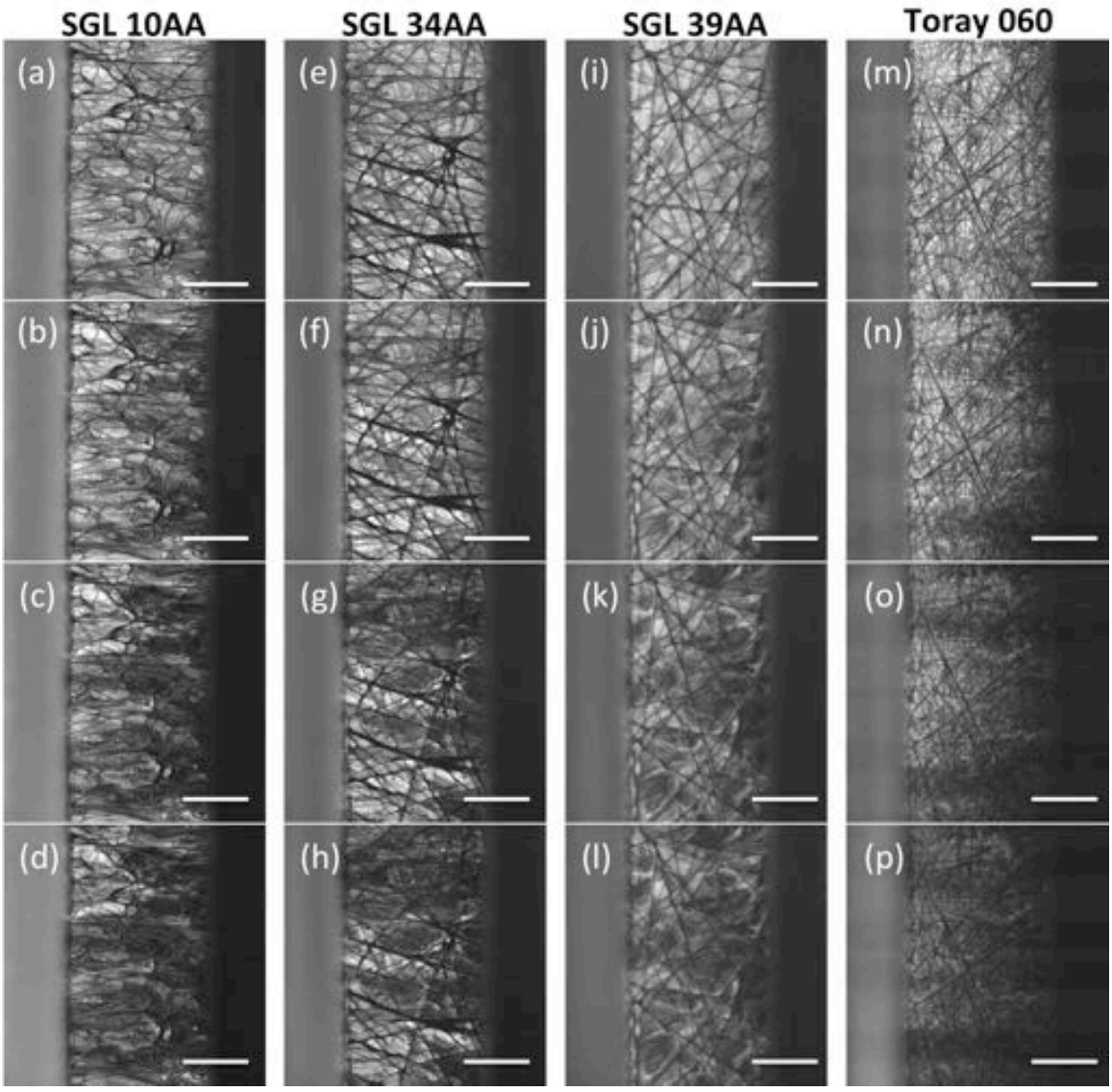

Figure 4. Fluorescence microscope images during the natural pulsation of the posolyte peristaltic pump. All scale bars are 1 mm. (a-d) SGL 10AA with characteristic looping filaments. (c) and (d) show bright regions of H_2AQDS stagnation and dark regions of fresh AQDS advection. (e-h) SGL 34 AA, similarly (e) shows relatively uniform H_2AQDS distribution within electrode pores while (g) and (h) show distinct regions of stagnation. (i-l) SGL 39 AA, (k) H_2AQDS is visibly generated on electrode filament and removed by advection. (m-p) Toray 060, more uniform advection, but still some slight channeling exists.

Even with different fiber morphology, fluorescence microscopy on the SGL 34AA paper tells a similar story, with the rapid fluid flow image (Fig. 4(h)) showing significant banding as the fluid preferentially penetrates certain portions of the porous electrode. However, SGL 39AA, which has a similar morphology to SGL 34AA, displays a distinctively different advection-driven flow profile (Fig. 4(l)) where the reduced H_2AQDS is noticeably generated on the fiber surface before being swept away in the pores further from the fibers. This is in contrast to the Toray 060 ((Fig. 4(o) and (p)) where H_2AQDS in not concentrated at the fiber surface but rather is visibly pushed by advection through the pores.

Figure 5 further highlights the stark heterogeneities in the fluid flow profile and electrochemical activity present within each of these commercial carbon electrodes. Each of these images is captured while oxidized AQDS is being pushed through the electrode and the same reducing current is being applied. It is evident across these images that modeling any these electrodes as a homogeneous porous conductor will not capture the reality of these meso-scale features. Again, even though the fiber morphology of SGL 10AA (Fig. 5(a)) and SGL 39AA (Fig. 5(b)) are significantly different, similar observations of bright stagnant regions of H_2AQDS accumulation and dark AQDS advection are made within the two electrodes. Furthermore, contrasting SGL 39AA (Fig. 5(c)) and Toray 060 (Fig. 5(d)), which, from Figure 2 have similar morphologies, it is evident that the advection of fluid is dramatically different between the two. The differences in these properties could be due to a number of factors including surface wettability and through-plane electrode morphology.

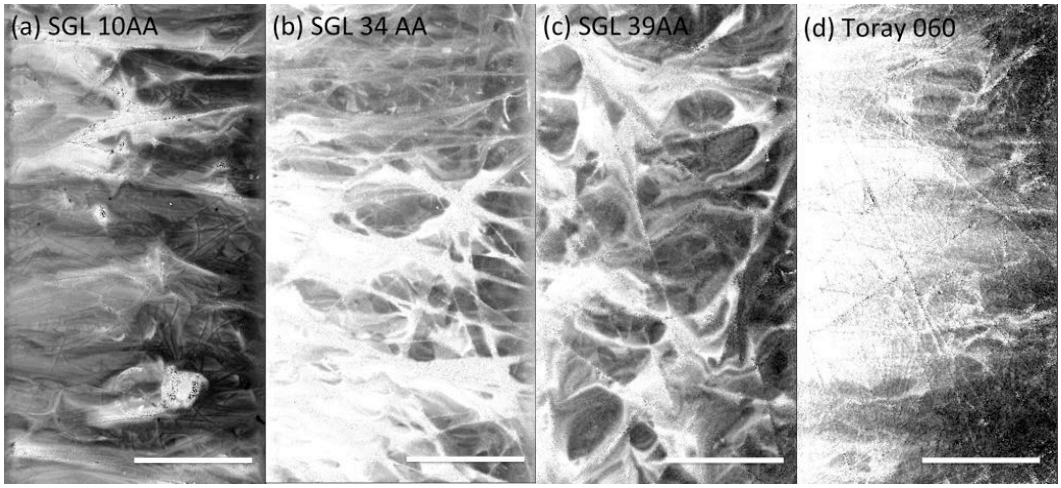

Figure 5. Fluorescence microscope images of the four commercial carbon electrodes. All scale bars are 1 mm, with inlet (right) and outlet (left). (a) SGL 10AA showing horizontal banding indicating heterogeneous fluid flow. (b) SGL 34AA showing region of stagnation (bottom left). (c) SGL 39 AA, reduced H_2AQDS generated at the carbon filament surface. (d) Toray 060 displays a different fluorescence map profile then any of the other electrodes.

Electrode-Flow Field Overlap

Given that these commercial porous carbon electrodes clearly have surprisingly heterogeneous properties, it raises the question of how the flow field geometry distributing fluid to the electrode might impact the performance of the electrochemical system. Figure 6 shows the reaction-flow map of the inlet finger of the IDFF over an

SGL 10AA carbon paper. This image was taken at steady state fluid flow with steady state reduction current. Distinct dark channels extending vertically and horizontally from the digit end show regions that are more rapidly refreshed by advection of oxidized AQDS. It is interesting to note that while the inlet channel has a dark region of oxidized AQDS on its border, the channeling effect appears to be determined by the electrode properties. This result suggests that although it is important to design flow fields for optimized fluid distribution, the reactant utilization might be strongly dependent on the electrode geometry and morphology — suggesting that this, too, can be optimized.

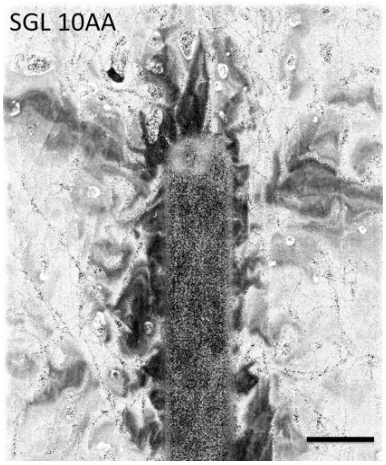

Figure 6. Fluorescence microscope image of the IDFF inlet channel end distributing oxidized AQDS into SGL 10AA carbon paper. Fluid flow and reduction current are constant. The dark regions are areas of more rapidly-refreshing AQDS and suggest pathways of lower pressure drops. Scale bar is 1 mm.

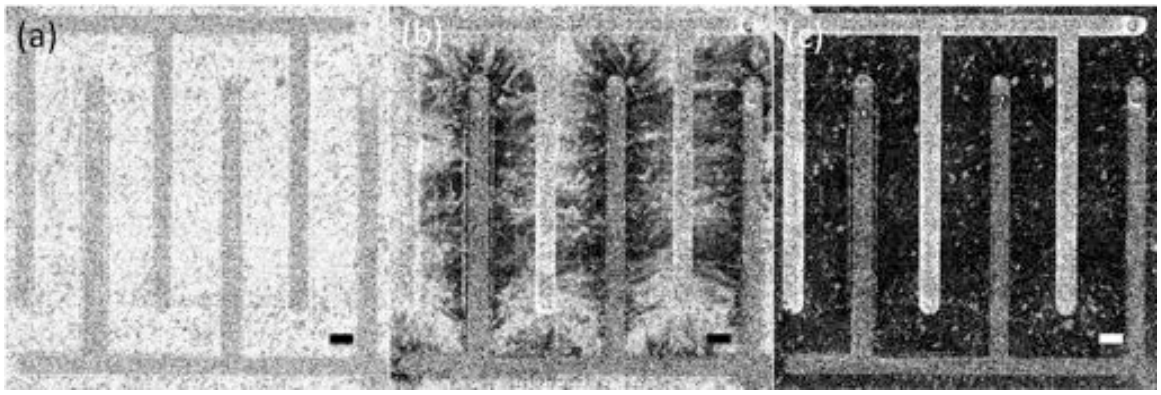

Figure 7. Fluorescence microscope images of the IDFF on top of SGL 10AA carbon paper. (a) Fully reduced H_2AQDS brightens the electrode area under the land. (b) Intermediate stage of oxidized AQDS flow to refresh electrode. Heterogeneous flow distribution remains evident at this scale. (c) Fully oxidized AQDS has completely refreshed the electrode. Outlet channels are brighter because of lingering reduced H_2AQDS. All scale bars are 1mm.

Zooming out even further, Figure 7 captures the full 2 cm^2 IDFF over an SGL 10AA carbon paper. This shows that fluorescence microscopy can be used as a valuable *in situ* technique with the capability of spanning multiple length scales from the microstructure to the macrostructure. Figure 7(a) and (c) show the electrode with fully reduced H_2AQDS, and fully oxidized AQDS respectively. In Figure 7(c) the channels are brighter from

previously reduced H_2AQDS. Figure 7(b) shows the transition period as AQDS is pumped into the cell, replacing H_2AQDS. Even at this scale, the flow heterogeneity between the inlet and outlet channels is clearly visible and even stagnation effects near the ends of the channels are evident.

Summary

There are several takeaways from these observations: 1. Fluid flow profiles and electrochemical reactions within porous electrodes are surprisingly heterogeneous on the length scales of tens of microns to millimeters. This will likely have a measurable effect on the performance of electrochemical systems such as flow batteries. 2. Commercial carbon papers, even from the same vendor, have starkly different flow-reaction properties at the pore scale. This indicates that bulk properties such as porosity, permeability, and conductivity and micro-scale properties such as surface area and catalyst coverage only tell part of the story. Clearly there is a greater need for understanding the structure-function properties relationships of porous carbon electrodes within electrochemical systems. Furthermore, this work shows how using fluorescence microscopy *in operando* opens the possibility of evaluating engineered high-performance porous electrodes. Custom designed electrodes in tandem with tailored flow fields, membranes, and reactants could push the envelope for high power density electrochemical systems.

Acknowledgments

This work was funded in part by the U.S. Department of Energy contract DE-AC05-76RL01830 through Pacific Northwest National Laboratory subcontract 304500, by the Massachusetts Clean Energy Technology Center, and by the Harvard John A. Paulson School of Engineering and Applied Sciences.

References

1. G. L. Soloveichik, *Am. Chem. Soc.*, **115**, 11533-11558 (2015).
2. M. L. Perry, A. Z. Weber, *J Electrochem Soc*., **163**(1), A5064-A5067 (2015).
3. M. Park, L. Ryu, W. Wang, J. Cho, *Nat Rev Mater*., **2**, 16080 (2016).
4. J. Winsberg, T. Hagemann, T. Janoschka, M.D. Hager, U.S. Schubert, *Angew. Chemie. – Int. Ed.*, **55**, 2-28 (2016).
5. A. Bazylak, *Int. J. Hydrogen Energy*, **34**(9), 3845-3857 (2009).
6. J. H. Park, J. J. Park, O. O. Park, C. S. Jin, J. H. Yang, *J. Power Sources*, **310**, 137-144 (2016).
7. V. Yarlagadda, T. Van Nguyen, *ECS Trans*., **58**(36), 25-32 (2014).
8. I. Mayrhuber, C. R. Dennison, V. Kalra, E. C. Kumbur, *J. Power Sources*, **260**, 251-258 (2014).
9. D. Yuan, Y. G. Zhu, C. Jia, in Carbon Nanotubes - Current Progress of their Polymer Composites, Ch. 17 Carbon Nanotube-Polymer Composites for Energy Storage Applications, InTech Open (2016).
10. L. Wei, T. S. Zhao, L. Zeng, Y. K. Zeng, H. R. Jiang, *J. Power Sources*, **341**, 318-326 (2017).
11. T. Liu, X. Li, C. Xu, H. Zhang, *ACS Appl. Mater. Interfaces*, **9**(5), 4626-4633, (2017).
12. J. J. Park, J. H. Park, O. O. Park, J.H. Yang, *Carbon,* **110**, 17-26 (2016).

13. Z. Zhang, J. Xi, H. Zhou, X. Qiu, *Electrochim. Acta*., **218**, 15-23 (2016).
14. G. Qiu, C. R. Dennison, K. W. Knehr, E. C. Kumbur, Y. Sun, *J. Power Sources*, **219,** 223-234 (2012).
15. G. Qiu, A.S. Joshi, C. R. Dennison, K. W. Knehr, E. C. Kumbur, Y. Sun, *Electrochim. Acta*., **64**, 46-64 (2012).
16. B. Huskinson, M. P. Marshak, C. Suh, et al., *Nature*, **505**(7482), 195-198 (2014).
17. K. Lin, Q. Chen, M.R. Gerhardt, et al., *Science,* **349**(6255), 1529-1532 (2015).
18. C. Qing, M. R. Gerhardt, L. Hartle, M. J. Aziz, *J. Electrochem Soc*. **163**(1), A5010-A5013 (2016).
19. L. Hoober-Burkhardt, S. Krishnamoorthy, B. Yang, et al., *J. Electrochem Soc*. **164**(4), A600-A607 (2017).
20. R.M. Cory, D.M. Mcknight, Environ. Sci. Technol., **39**, 8142-8149 (2005).
21. J. T. Clement, D. S. Aaron, M. M Mench, *J. Electrochem. Soc*., **163**(1), A5220-A5228 (2016).